
Numerical Simulation of Electron Beam Welding and Instrumental Technique

**Muriel Carin — Philippe Rogeon — Denis Carron
Philippe Le Masson — Daniel Couëdel**

*Laboratoire d'Etudes Thermiques Energétique et Environnement
Université de Bretagne Sud - Centre de Recherche
Rue de Saint Maudé
F-56321 Lorient cedex
muriel.carin@univ-ubs.fr*

ABSTRACT. In the present work, thermal cycles measured with thermocouples embedded in specimens are employed to validate a numerical thermometallurgical model of an Electron Beam welding process. The implemented instrumentation techniques aim at reducing the perturbations induced by the sensors in place. The numerical model is based on the definition of a heat source term linked to the keyhole geometry predicted by a model of pressure balance using the FEMLAB code. The heat source term is used by the thermometallurgical simulation carried out with the finite element code SYSWELD. Kinetics parameters are extracted from dilatometric experiments achieved in welding austenitization conditions at constant cooling rates.

RÉSUMÉ. Dans cette étude, on valide un modèle numérique du soudage par faisceau d'électrons à l'aide de cinétiques thermiques mesurées dans des éprouvettes instrumentées en thermocouples. Les techniques d'instrumentation mises au point visent à limiter les perturbations inévitables générées par l'intrusion des capteurs. Le modèle numérique est basé sur la définition d'un terme source lié à la géométrie du capillaire de vapeur prédite par un modèle d'équilibre des pressions utilisant le logiciel FEMLAB. Ce terme source est introduit dans le modèle thermométallurgique utilisant le code SYSWELD. Les paramètres des cinétiques métallurgiques sont obtenus à partir d'essais dilatométriques réalisés dans des conditions d'austénitisation proches de celles du soudage et avec des vitesses de refroidissement maintenues constantes. Les résultats numériques sont comparés avec les résultats expérimentaux obtenus pour un acier 16MnNiMo5.

KEYWORDS: electron beam welding, temperature measurement, metallurgy, transformation kinetics, thermal modelling, keyhole, recoil pressure.

MOTS-CLÉS: soudage par faisceau d'électrons, mesure de température, métallurgie, cinétiques de transformation, modélisation thermique, capillaire de vapeur, pression de recul.

1. Introduction

High power density welding technologies, such as Electron Beam (EB) welding, have the advantage to produce welds with high aspect ratio (depth-to-width ratio) and narrow heat-affected zone, compared with conventional welding processes. Due to the lack of a predictive tool, welding parameters are still adjusted experimentally. To facilitate the optimization of the welding parameters, it is desirable to develop numerical tools that can be used as a predictive capability for the welding process. As such process involves complex physical mechanisms inducing interactions between thermal, mechanical and metallurgical phenomena, the numerical simulation of welding process is still a challenging task. In particular, the validation of numerical models needs reliable experimental thermal histories. However in the case of thick specimen, as it is difficult to insert deeply the thermocouples, the comparison between predictions and experiment is most often restricted to the examination of macrographs and weld joint shapes. Some authors have attempted to measure temperature in large pieces by embedding thermocouples in drilled holes in large pieces (Costantini, 1996), Grignon et al., 2001). But this technique can lead to imprecise measurements especially due to an inaccurate sensor position and the large size of sensors used. We propose here an innovating method of embedding micro-thermocouples inside thick and large specimens. Bulk specimens are first sectioned to allow the implantation of temperature sensors on the interfaces and then rejoined before welding. Two experiments of partial penetration weld were performed on two types of specimens. These results are used to validate our numerical model.

2. Experimental setup

2.1. Preliminary tests

In the case of thick and large specimens, the embedding of thermocouples in region close to the weld joint is technically difficult. Furthermore the fusion zone (FZ) and the heat-affected zone (HAZ) are very narrow for this type of welding. The technique of embedding, necessarily intrusive, must be as less disturbing as possible which implies the use of fine wire thermocouples inserted in small holes. The location of the measuring junction is crucial. All these constraints make difficult the access to the HAZ by drilling. We propose here a method of embedding thermocouples based on the cutting of the specimen and a fine instrumentation of slices.

The weld joints have been made on 16MnNiMo5 steel samples, provided by the CRMC¹ laboratory (ARCELOR). The welding experiments were performed at the DCN INDRET² using a non-vibrating electron beam in high vacuum. The following welding parameters were used: accelerating voltage $U = 60$ kV, beam current $I = 290$

1. Centre de Recherche des Matériaux du Creusot, Arcelor, Le Creusot, France.

2. Direction des Constructions Navales d'Indret, Nantes, France.

mA, welding speed $V = 2.5 \text{ mm}\cdot\text{s}^{-1}$, focus current $I_f = 2.46 \text{ A}$, working distance $dt = 160 \text{ mm}$ (distance from the top of the chamber to the top of the work piece).

Two different types of cutting were investigated: the specimen was sectioned longitudinally or transversally (Figure 1a,b). In order to show the negligible effect of the cutting on the shape of the weld joint, welding tests were performed on two reconstituted specimens. After cutting, the surfaces were rectified, the slices were fitted together, and then joined by arc welding on the edges, in order to reconstitute the entire specimen prior to welding. The macrographs of weld joints obtained for both reconstituted specimen were compared with the macrograph of an uncut test weld joint (Figure 1 c, d, e).

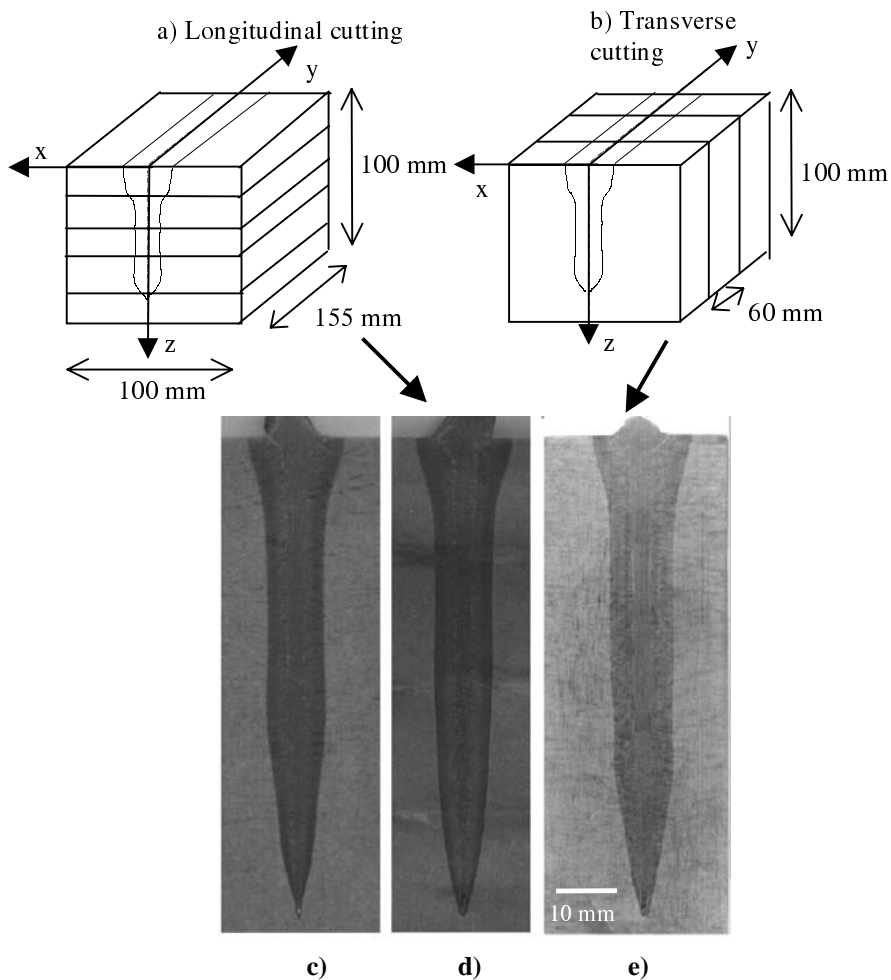


Figure 1. Schematic of the cut specimens (a, b), photographs of weld cross-sections (uncut test specimen (c), longitudinal cut specimen (d), transverse cut specimen (e))

The good correlation between the three weld joints in terms of size and shape of HAZ and FZ demonstrates the negligible influence of the interfaces on the welding process.

2.2. Thermocouple embedding

The macrograph of the uncut test weld (Figure 1c) was used to define the future location of the thermocouples in HAZ or base metal. Two specimens were embedded with thermocouples: specimen 1 (longitudinal cutting) and specimen 2 (transverse cutting). Different types of thermocouples of small diameter (80 μm), K-type (Chromel-Alumel $T < 1250^\circ\text{C}$), C-type (Tungsten-Rhenium $T < 2300^\circ\text{C}$) and S-type (Platinum-Rhodium $T < 1750^\circ\text{C}$) were tested. In order to reduce thermal losses from the wires and avoid perturbations due to interfaces, the measuring junctions were inserted inside holes (2 mm depth and 0.5 mm diameter) drilled into the plates. Therefore the temperature is measured inside the plate rather than at the interface surface. The thermocouple junctions were welded by capacitive discharge at the bottom of cone-shaped holes (Figure 2-1), which were filled with high thermal conductivity ceramic adhesive (Aremco Ceramabond 571) (Figure 2-2). The thermocouple wires were inserted in alumina protection tubes (0.63 mm diameter) and placed in milled channels (0.8 mm depth) filled with ceramic adhesive (Figure 2-3,4,5,6). The handling of C or S-type thermocouple wires is not an easy task since the C-type thermocouples are very fragile and the S-type thermocouples are very ductile. After embedding, the surfaces were rectified and the specimen was reconstituted.

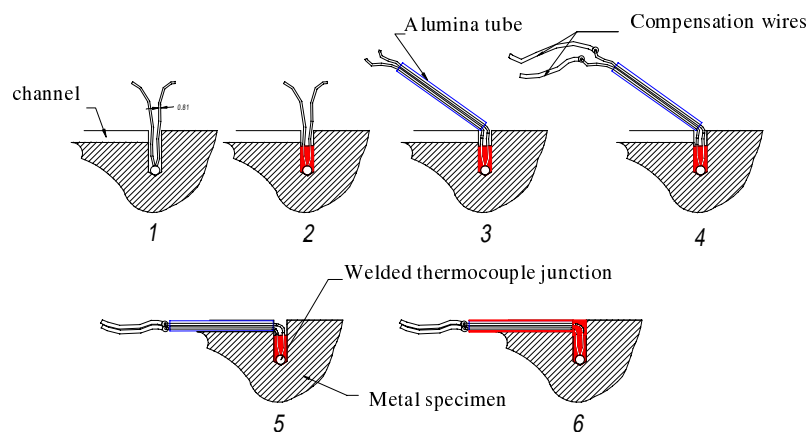


Figure 2. Embedding of a thermocouple in a specimen

3. Definition of the numerical model

3.1. Introduction

The goal of this study is to propose an experimental method to validate a numerical model in term of thermal history in HAZ. Here the numerical model will be restricted to a thermometallurgical model, ignoring the hydrodynamic phenomena in the molten pool and assuming a two-dimensional approach. The interaction between the electron beam and the metal will be modelled by a moving heat source. Two calculations are performed: a transient calculation in the 2D transverse (x,z) plane and a quasi-stationary calculation in the 2D longitudinal (x,y) plane (Figure 3). The thermometallurgical simulation is carried out using the SYSWELD³ finite element computer software, which deals with the thermometallurgical linkage through the non-linear heat transfer equation and the metallurgical kinetic equations described in Rogeon et al. (1999). In this work, the metallurgical models employed are Leblond-Devaux for the diffusional transformations and Koistinen-Marburger for martensitic transformation (Leblond et al., 1984). The main inputs used for the calculation are:

– the thermophysical properties of 16MnNiMo5 (ASTM A508 Cl.3) steel for various phases. The model takes into account temperature dependent properties and the latent heat of fusion and evaporation of the metal. The temperature-dependent density ρ , thermal conductivity λ and heat capacity C are given in tables 1 and 2.

T (°C)	20	100	200	300	400	500	600	650	700
$\rho(\text{kg.m}^{-3})$	7850	7825	7800	7770	7740	7700	7660	7640	7620
$\lambda(\text{W.m}^{-1}\text{°C}^{-1})$	52	49	46.5	43.5	41	38	35	33	32
$C(\text{J. kg}^{-1}\text{°C}^{-1})$	470	490	525	565	615	680	770	815	850

Table 1. Thermophysical properties of α -phase

T (°C)	200	300	400	500	600	700	800	900	1000
$\rho(\text{kg.m}^{-3})$	7950	7900	7850	7800	7750	7700	7650	7600	7550
$\lambda(\text{W.m}^{-1}\text{°C}^{-1})$	17.5	18.25	19.75	21	22.5	23.5	24.5	26	27.5
$C(\text{J. kg}^{-1}\text{°C}^{-1})$	530	545	560	570	580	590	600	620	630

Table 2. Thermophysical properties of γ -phase

3. SYSWELD, finite element code distributed by ESI Group.

– the chemical composition of 16MnNiMo5 steel: (0.153 C, 1.330 Mn, 0.252 Si, 0.739 Ni, 0.241 Cr, 0.521 Mo, 0.063 Cu, 0.006 S, 0.007 P, 0.026 Al, 0.007 V; by wt. percent).

– the parameters of the metallurgical laws for the phase transformations during heating and cooling. These parameters were deduced from dilatometric experiments performed on a Gleeble machine (see details on experiment in Carron et al., 2002). Two austenitizing conditions similar to those encountered in the HAZ were considered: a heating rate of 1000°C/s with a peak temperature $T_{\text{peak}} = 1200^{\circ}\text{C}$ (grain coarsened region of the HAZ) and a heating rate of 300°C/s with $T_{\text{peak}} = 950^{\circ}\text{C}$ (grain refined region of the HAZ). Various cooling rates (from 1 to 80°C/s) were achieved. The choice of the set of metallurgical parameters used in the simulation will be discussed in section 4.3.

– a heat source model described in details in Rogeon et al. (1999) which consists of two elements: a ring shaped surface heat source and a cylindrical volume heat source with uniform energy distribution along the depth (figure 3). The dimension (height and diameter) of the cylindrical source is deduced from the shape of the keyhole calculated with a mechanical model detailed hereafter.

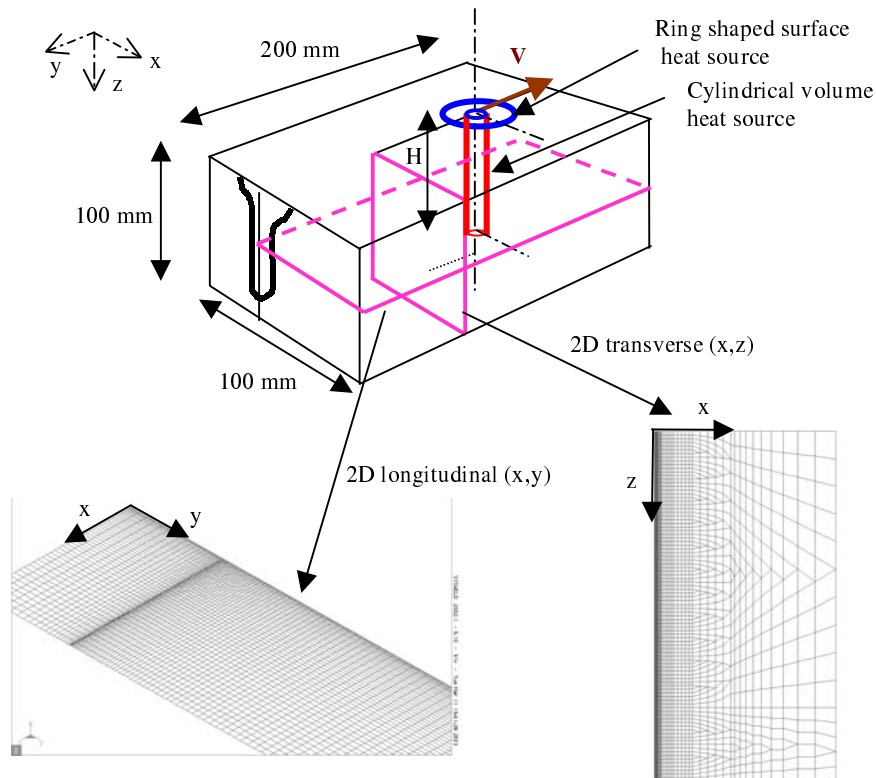


Figure 3. Schematic of the geometry of the Finite Element model and the two meshes used in SYSWELD

3.2. Mechanical model for the keyhole

During high-energy-density welding processes, such as laser and electron beam, the melt surface undergoes large deformations, the energy is then deposit in depth leading to high penetration depth. Generally this maximum penetration depth is reached when the equilibrium of the keyhole is assumed to be achieved. There are currently two types of model that address the issue of prediction of keyhole shape: the first is based on heat balance, the second on a pressure balance. In the energetic approach, the shape is deduced from a balance between the absorbed power transferred to the keyhole wall and the heat losses such conduction, convection or evaporation losses (Rosenthal, 1946; Jüptner, 1975; Noller, 1983, Kaplan, 1994). Conduction losses are generally calculated from the two-dimensional moving-line-source or the solution for a cylindrical or elliptical cavity moving through an infinite plate. The mechanical approach is based on the balance of evaporation recoil pressure and sum of hydrodynamic pressure, hydrostatic pressure due to gravity and pressure due to surface tension (Andrew *et al.*, 1976; Dumord, 1996) by assuming a steady-state keyhole. Some authors have also attempted to calculate iteratively the keyhole radius and surface temperature by satisfying both heat and pressure balance (Wei *et al.*, 1990; Kroos *et al.*, 1993, Solana *et al.*, 1997). Recently, the assumption of a steady-state keyhole has been questioned by some authors in the case of laser welding (Matsunawa *et al.*, 1997; Semak *et al.*, 1997; Fabbro *et al.*, 2000). In this case, the keyhole is essentially non-stationary and remains in the state of growth resulting in a drilling-like propagation of the keyhole in the material. They have proposed transient models for the keyhole during laser welding able to predict keyhole instabilities consistent with experimental observations (Semak *et al.*, 1999; Fabbro *et al.* 2000). More sophisticated models requiring much more time-consuming calculations have recently been developed. They take into account the coupling between hydrodynamic and heat transfer and use a specialized method to deal with the presence of the free surface of the liquid-vapour interface in a transient 3D model (Ki *et al.*, 2001; Rabier, 2003). However such models are still limited to small deformations of the keyhole (few millimeters) generally applied to laser welding. In this work, we are interested in electron beam welding experiment performed in an evacuated chamber under vacuum resulting in high maximum keyhole depth (around 75 mm). In such conditions, the position of the focus point relative to the sample surface has a strong influence on the penetration depth which is generally not taken into account in models applied to laser welding. An important feature of our model is the consideration of the variation of the absorbed energy with the depth z in order to account for this effect.

In the electron beam process considered here, the welding speed is relatively slow ($2.5 \text{ mm}\cdot\text{s}^{-1}$). The characteristic time is then of order 0.2 s for a beam radius of 0.5 mm which is much higher than the keyhole formation time 1-50 ms for drilling a keyhole (Miyazaki, 1977; Matsunawa *et al.*, 1997). So the assumption of a quasi-steady keyhole seems reasonable. Furthermore we assume that the keyhole is held open due to a pressure balance. At this stage of investigation, we have chosen to

ignore the hydrodynamic pressure due to the fluid flow around the keyhole. Since the process of energy transfer is still not completely understood in electron beam, we assume that there is no reflection and that all of the incident power absorbed by the keyhole surface is used to evaporate the metal, as a first approximation. The pressure balance between the recoil pressure P_{recoil} , the pressure due to surface tension P_{σ} and the hydrostatic pressure P_g is then:

$$P_{\text{recoil}} + P_{\sigma} + P_g = 0 \quad [1]$$

Recoil pressure

The recoil pressure is given by the expression proposed by Matsuiro *et al.* (1994), which is based on the conservation of momentum at the interface liquid – vapour leading to an expression for the vapour jet velocity and on the local energy balance equation to calculate the ejected mass. The recoil pressure is then given by :

$$P_{\text{recoil}} = \frac{(\Delta\varphi)^2}{\rho_{\text{gaz}} \Delta H_v} \quad [2]$$

where ρ_{gaz} is the vapour density (kg.m^{-3}), $\Delta\varphi$ is the absorbed electron beam intensity (W.m^{-2}) and ΔH_v is the latent heat of evaporation (J.kg^{-1}). When no reflection occurs and all of the incident beam energy is used for evaporation, the absorbed intensity is defined as:

$$\Delta\varphi = \Delta\varphi_{\text{inc}} \cos(\theta) \quad [3]$$

where $\Delta\varphi_{\text{inc}}$ represents the incident beam intensity and θ the angle between the beam axis and the local normal to the keyhole wall surface.

The beam intensity is assumed to be a Gaussian distribution at any transverse cross-section with perfect electron optics which can be expressed as:

$$\Delta\varphi_{\text{inc}}(r, z) = \frac{UI}{2\pi\omega_z^2(z)} \exp\left(-\frac{r^2}{2\omega_z^2(z)}\right) \quad [4]$$

where U is the voltage (V), I is the beam current (A), ω_z is the standard deviation of the energy distribution at a given depth z (m) and r is the polar coordinate (distance from beam axis) (m).

The variation of the standard deviation with the coordinate z is given by the formula :

$$\omega_z^2(z) = \omega_0^2 + \alpha^2(z - z_0)^2 \quad [5]$$

where ω_0 and α are the standard deviation at the focus plane and the beam angle respectively, z_0 is the position of the focus plane relative to the sample surface (z_0 is positive if the focus plane is below the sample surface located at $z = 0$). The recoil pressure can then be expressed as:

$$P_{\text{recoil}}(r, z) = \frac{(UI \cos(\theta))^2}{4\pi^2 \omega_z^4(z) \rho_{\text{gaz}} \Delta H_v^2} \exp\left(-\frac{r^2}{\omega_z^2(z)}\right) \quad [6]$$

If the hydrodynamic pressure and conduction losses are neglected, the problem becomes axisymmetric. The geometry of the keyhole can be described by a function $z(r)$. We can write :

$$\cos(\theta) = \frac{1}{\sqrt{1 + (dz/dr)^2}} \quad [7]$$

$$\text{Hence, } P_{\text{recoil}}(r, z) = \frac{(UI)^2}{4\pi^2 \omega_z^4(z) \rho_{\text{gaz}} \Delta H_v^2 (1 + (dz/dr)^2)} \exp\left(-\frac{r^2}{\omega_z^2}\right) \quad [8]$$

Pressure due to surface tension

The pressure due to surface tension P_σ is equal to the product of the surface tension coefficient σ (N.m^{-1}) and the curvature κ . For an axisymmetric surface, the curvature can be expressed as:

$$\kappa(r, z) = \frac{1}{r} \frac{d}{dr} \left(\frac{r (dz/dr)}{\sqrt{1 + (dz/dr)^2}} \right) \quad [9]$$

The pressure P_σ is then:

$$P_\sigma(r, z) = \sigma \frac{1}{r} \frac{d}{dr} \left(\frac{r (dz/dr)}{\sqrt{1 + (dz/dr)^2}} \right) \quad [10]$$

For small deformation of the surface keyhole, the curvature can be approximated by :

$$\kappa(r, z) = \frac{1}{r} \frac{d}{dr} \left(r \frac{dz}{dr} \right) \quad [11]$$

Hydrostatic pressure

The hydrostatic pressure P_g due to gravity is written in the classical form :

$$P_g(z) = -\rho_{\text{liq}} g z \quad [12]$$

where ρ_{liq} is the density of the liquid metal (kg.m^{-3}) and g is the gravitational acceleration (m.s^{-2}). Finally, we can re-write equation (1) to obtain equation (13) :

$$\begin{aligned} -\sigma \frac{1}{r} \frac{d}{dr} \left(\frac{r (dz/dr)}{\sqrt{1+(dz/dr)^2}} \right) + \rho_{\text{liq}} g z \\ = \frac{(UI)^2}{4\pi^2 \omega_z^4(z) \rho_{\text{gaz}} \Delta H_v^2 (1+(dz/dr)^2)} \exp\left(-\frac{r^2}{\omega_z^2(z)}\right) \end{aligned} \quad [13]$$

This equation is completed by the following boundary conditions:

$$\text{– at } r = 0: \frac{dz}{dr} = 0,$$

– at $r = L$: $z = 0$, where L is the length of the domain.

Since equation (13) is highly nonlinear, it was solved using the simulation tool FEMLAB® by choosing Hemholtz's equation in 1D. FEMLAB is a commercial software using the finite element analysis to solve differential equations. FEMLAB® is available commercially (<http://www.femlab.com/>) and is presented in Van Schijndel (2003).

A domain of 5 mm long was discretized in 52 Lagrange quadratic elements refined near $r = 0$. The properties used for the calculation are given in Table 3. The electron beam characteristics (ω_0 and α) were measured from the Arata Beam test performed on 0.1 mm thick tungsten strips (Arata 1986).

Liquid metal density	$\rho_l = 7200 \text{ kg.m}^{-3}$
Vapour density	$\rho_g = 0.25 \text{ kg.m}^{-3}$
Latent heat of evaporation	$\Delta H_v = 6.084.10^6 \text{ J.kg}^{-1}$
Surface tension coefficient	$\sigma = 1 \text{ N.m}^{-1}$
Gravitational acceleration	$g = 9.81 \text{ m.s}^{-2}$
Voltage	$U = 60000 \text{ V}$
Beam current	$I = 0.29 \text{ A}$
Beam radius at the focus plane	$\omega_0 = 0.09 \text{ mm}$
Beam angle	$\alpha = 0.014 \text{ rad}$

Table 3. Calculation parameters

The influence of the focus plane on the maximum depth is presented in Figure 4. The model predicts an optimal penetration for a focus plane located into the sample corresponding to $z_0 = 55$ mm. The evolution of the maximum penetration with the focal distance is consistent with previous experimental works (Konkol *et al.*, 1971; Jüptner, 1975; Giedt *et al.*, 1988; Jin *et al.*, 2003). This justified the expression of the recoil pressure that accounts for the variation of beam intensity with the z -coordinate. It can be seen in Figure 4 that if the curvature is approximated with equation 11, the keyhole depth is much smaller especially in the range of the optimal depth, which corresponds to welding conditions generally used in practice. Thus to predict realistic keyhole depth, it is necessary to calculate accurately the curvature of the keyhole surface. In the welding experiment presented here, the focus plane was located at 50 mm below the sample surface. This led to a weld joint with a height of 74 mm (figure 1), which is in a good agreement with the theoretical keyhole depth. However, further experiments are required to validate this mechanical model at different focus plane locations.

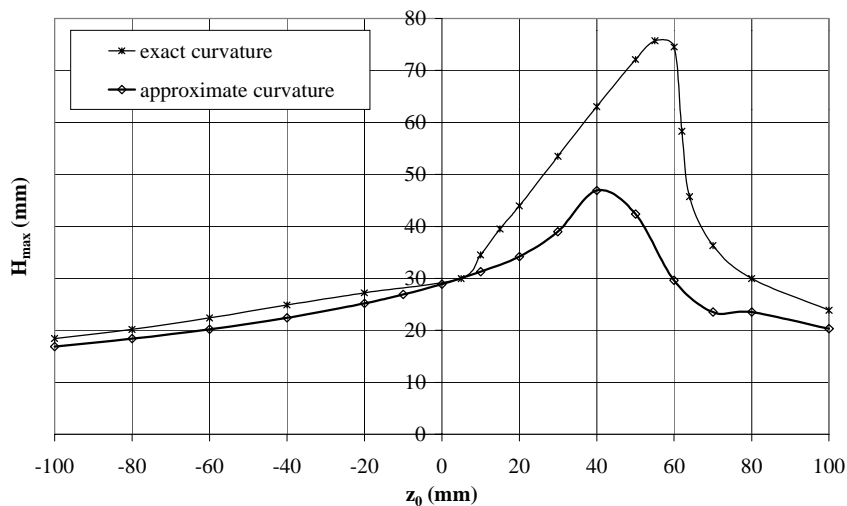


Figure 4. Maximum depth of the keyhole as a function of the focus plane z_0 with $U = 60000$ V, $I = 0.29$ A, $\alpha_0 = 0.09$ mm, $\alpha = 0.014$ rad. Influence of the curvature approximation

4. Experimental validation of the numerical model

4.1. Transverse plate assembly

Figure 5 shows the plates embedded with 8 thermocouples (4 K-type, 2 S-type and 2 C-type), 4 thermocouples are located in the future HAZ and the others in the base metal. The sensors are placed symmetrically along the weld line, in order to validate the experimental measurements and also check the stability of the weld line direction.

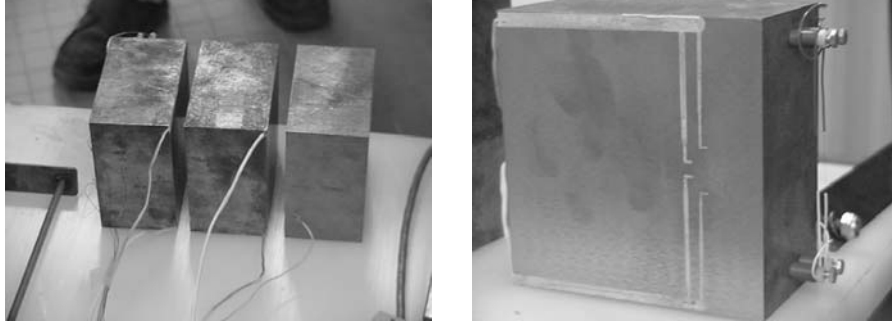


Figure 5. (a) the three plates before assembly, (b) : middle plate with thermocouple channels

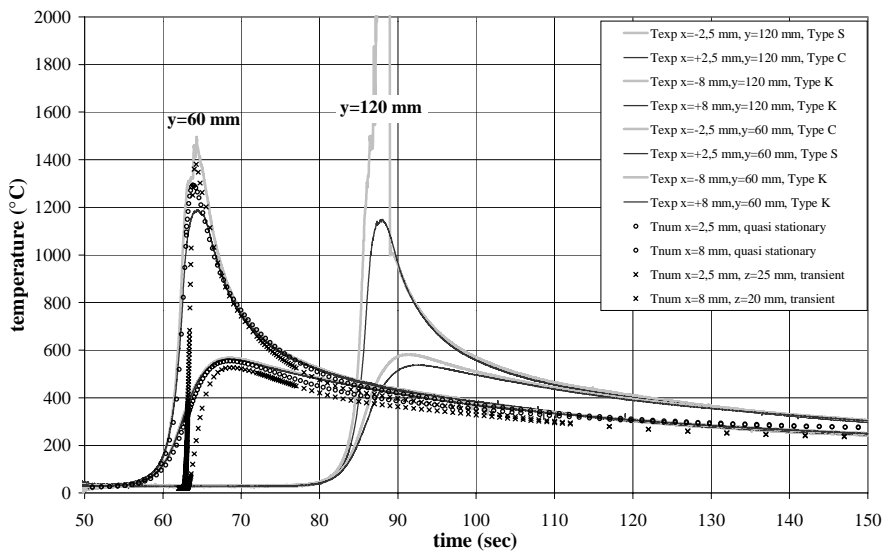


Figure 6. Temperature profiles at different locations and a comparison between the calculated (*Tnum*) and experimental (*Texp*) temperatures at $y = 60$ mm

The temperatures were monitored by a data acquisition system via an analog/digital data acquisition board (Iotech DaqBoard 216, 16 bit) and by a multiplexer/signal conditioner (Iotech DBK 19) at a 100 Hz frequency. Concerning the experimental results, all monitored signals provide exploitable data (Figure 6) and the macrograph of the weld shows expected FZ and HAZ shapes (Figure 7). It can be noticed that a small asymmetry is observed for the first plate ($y = 60$ mm) that

4.2. Longitudinal plate assembly

A similar method of sensor embedding was carried out on a specimen cut in longitudinal plates. Three faces were instrumented with 38 thermocouples (20 K-type, 16 S-type and 2 C-type). Again the sensors were positioned symmetrically along the weld axis (Figure 8).

After monitoring, the only exploitable data stem from K-type thermocouples and one S-type thermocouple. Due to their high fragility, C-type or S-type thermocouples were broken during set up. The signals exhibit little noise and are of good quality (Figure 9). The good correlation between temperature profiles measured by the thermocouples located symmetrically along the weld line shows the good repeatability of measurement and the reliability of the location of the thermocouples (illustrated in Figure 9 for $x = \pm 4.5$ mm and $z = 40$ mm). The peak temperature exceeding 800°C confirms the position of thermocouples in HAZ. This is in agreement with the observation of the longitudinal cross-section macrograph (Figure 10c) in the plane of the measuring junctions ($z = 40$ mm) which enables to locate accurately the sensors in HAZ.

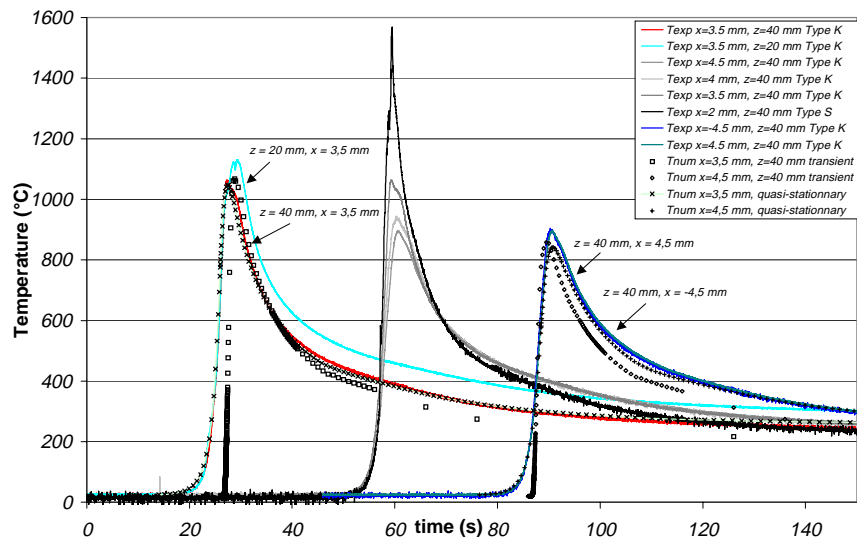


Figure 9. Comparison of temperature predictions and measurement at various locations

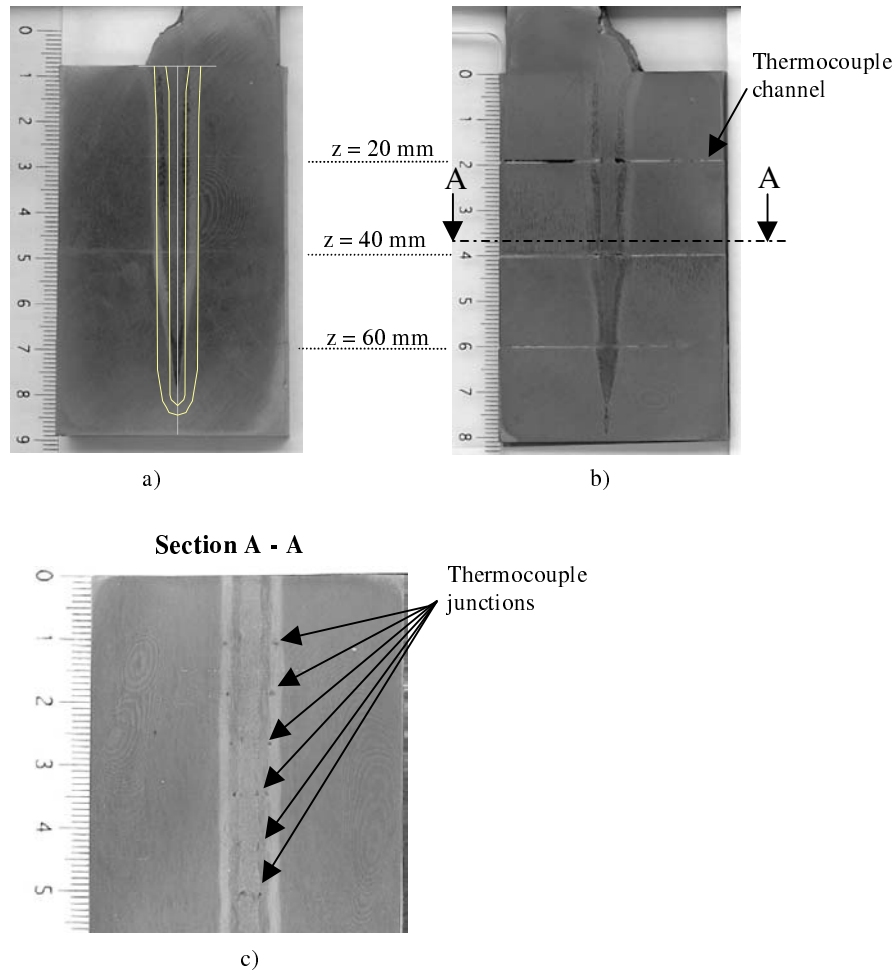


Figure 10. Transverse and longitudinal macrographs (a: transverse cross-section in a plane without thermocouple and predicted HAZ and FZ, b: transverse cross-section in the channel plane, c: longitudinal cross-section with thermocouples junctions ($z=40$ mm⁴))

As shown in Figure 10c, the width of the HAZ is around 10 mm and remains constant along the weld direction. This confirms the stability of the welding parameters and allows a comparison of thermal cycles regardless of the y-position.

4. Indeed, since the thermocouples are inserted into holes of 2 mm depth, the measured temperature corresponds to $z \approx 38$ mm. However, to simplify the writing, we will consider $z=40$ mm.

The experimental heating and cooling rates have been estimated from thermocouple signals located at $z = 40$ mm and various x -axis distances in the HAZ (table 4).

V (°C /s)	x = 2 mm		x = 3.5 mm		x = 4 mm		x = 4.5 mm	
	Exp	Num	Exp	Num	Exp	Num	Exp	Num
Heating Stage								
T [700 – 900°C]	746	680	403	380	239	180	197	160
Cooling Stage :								
T = 800°C	-60	-52	-59	-55	-53	-38	-45	-37
T = 500°C	-13	-14	-11	-15	-11	-15	-11	-14

Table 4. Thermal rates from experiment and FE quasi-stationary model during heating and cooling stages at $z=40$ mm

For a given depth ($z = 40$ mm), the heating rates in the austenitizing temperature range [700 - 900°C] reach a mean value of 746°C/s near the fusion zone and decrease in the HAZ thickness, down to 197°C/s near the base metal (table 4). During cooling, in the temperature range of bainitic metallurgical transformations [800 - 500°C], thermal kinetics depend strongly on temperature (from -60 to -13°C/s, near the fusion zone and from -45 to -11°C/s, near the base metal). However, cooling rates are nearly constant in the HAZ thickness (Table 4). Furthermore two temperature profiles obtained at different depths ($z = 20$ and 40 mm) and same x -axis distance ($x = 3.5$ mm) exhibit significant discrepancy (Figure 9). The peak temperature is higher at the top of the weld joint ($z = 20$ mm) with slower cooling rates (-47 °C/s at 800°C and -7 °C/s at 500°C). This indicates that the energy distribution is non-uniform along the depth, manifestly higher at the top of the weld. This can be related to the triangular shape of the weld joint, which can be attributed to a non-uniform energy distribution along the depth induced by the combined effects of non uniform surface energy deposit on the keyhole wall and the hydrodynamic phenomena in the molten pool.

Concerning the influence of the method of sensor embedding on the weld joint, longitudinal macrograph in the plane of the measuring junctions shows no effect on the shape of HAZ and fusion zone (Figure 10c). However transverse macrograph reveals local broadening of the fusion zone at the interface locations and more precisely at the extremities of thermocouple channels (Figure 10b). These perturbations can be attributed to the local change in thermal diffusivity. This observation justifies the precautions taken here, consisting in shifting the measurement perpendicularly to the interfaces in the bottom of small holes drilled into plates.

4.3. Comparison between experimental and numerical results

From an energetic point of view, the comparison between experimental and predicted HAZ and FZ geometries shows some discrepancies (Figures 7, 10a). The assumption of a uniform energy distribution in the volume heat source term, well suited in the case of cylindrical joint, does not permit to reproduce correctly the V-shaped weld observed here. Correlatively it was shown from the experimental thermal cycles measured at various depths that the energy decreases along the depth (Figure 9). Furthermore the typical ‘nail head’ shape, not well simulated here, indicates that the surface heat source is underestimated. Convective phenomena in the weld pool and radiative energy from metal vapour out of the keyhole could contribute to increase the energy at the top of the weld. However experimental and theoretical thermal cycles are in good agreement (Figures 6, 9) especially in the case of the 2D quasi-stationary (x,y) model. The thermal rates predicted by this model are also in good accordance with the experimental values (table 4). In the case of 2D transient model (x,z), the thermal kinetics are not well predicted particularly during heating stage due to the adiabatic assumption along y-axis ($\partial T/\partial y$ assumed negligible compared to $\partial T/\partial x$ and $\partial T/\partial z$) (Figures 6, 9, 11). However this model has the advantage to predict quenching effect occurring at the root of the weld, as shown by the increase of the cooling rates with the depth z (Figure 11). In view of the above, it is readily apparent that a 3D model is recommended in Electron Beam partial penetration welding simulation.

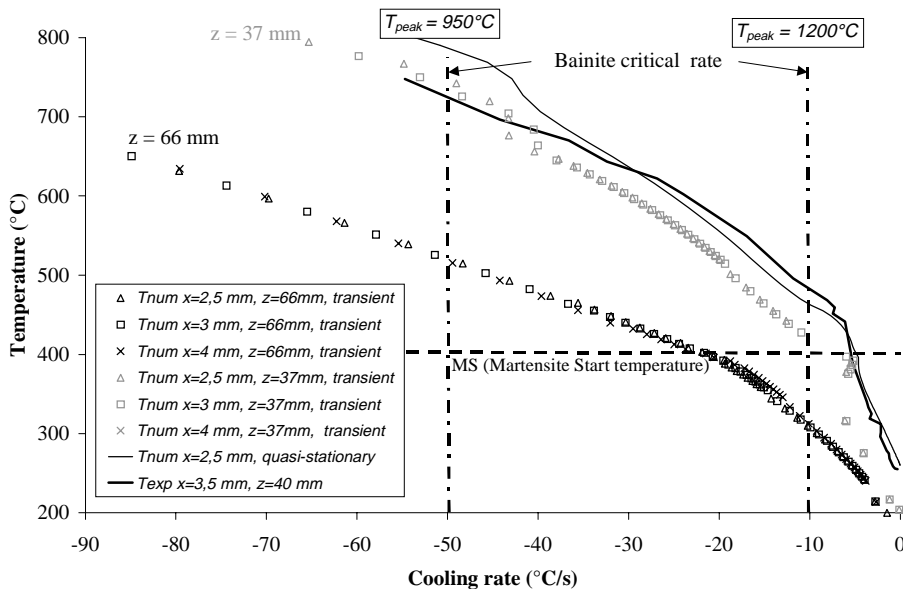


Figure 11. Comparison between experimental and theoretical thermal cooling rates near the root ($z = 66\text{ mm}$) and at the middle of the weld joint ($z = 37\text{ mm}$)

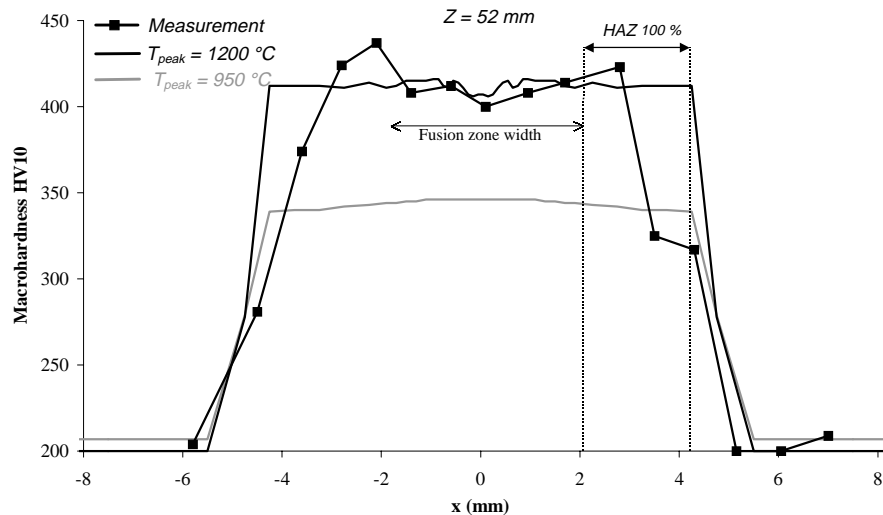


Figure 12. Experimental and theoretical macrohardness profiles at $z = 52$ mm. Influence of the set of metallurgical parameters

Concerning the metallurgical aspect, the predicted macrohardness is found constant in the fully austenitized part of the HAZ (HAZ 100%) with both set of metallurgical parameters ($T_{\text{peak}} = 950^{\circ}\text{C}$ or 1200°C), contrary to Vickers macrohardness measurements (HV10) (figure 12). These measurements have been carried out in the transverse cross-section plane of the weld joint at $z = 52$ mm and show that the macrohardness decreases with increasing distance from the weld centerline (y-axis). Nevertheless, the use of parameters corresponding to $T_{\text{peak}} = 1200^{\circ}\text{C}$ gives a better correlation in the grain-coarsened region whereas the parameters corresponding to a lower peak temperature gives a better correlation in the grain-refined region. As cooling rates are identical in the HAZ thickness (Figure 11 et table 4), when using only one set of parameters, the theoretical phases and thus hardness evolutions in the HAZ thickness depend only on the austenitizing rate (Figure 12). In the fully austenitized part of the HAZ, the theoretical hardness evolution is consequently uniform, contrary to experimental hardness evolution related to the prior austenitic grain size. Therefore, to predict accurately the microstructure in the entire HAZ thickness, precise dilatometric experiments established in different austenitizing conditions are required.

5. Conclusion

The development and validation of simulation tools to predict Electron Beam welding process require a good knowledge of the experimental thermal fields. We

proposed here a method of embedding thermocouples inside thick and large specimens. The specimens are first sectioned to allow a fine instrumentation of the interfaces and then reconstituted. It has been shown that the presence of interfaces has no effect on the weld joint. Welding tests were performed on two instrumented specimens cut in two directions: longitudinal (x,y) or transverse (x,z). The longitudinal cutting and transverse cutting favor respectively the analysis of thermal fields in the HAZ thickness along x -axis and in the depth along z -axis. The experimental signals recorded in the samples with low noise are found reproducible, showing the good quality of the instrumentation. They supply accurate values of thermal rates during heating and cooling stage and give information concerning the energy distribution along the depth.

Two bidimensional thermometallurgical models, a transient in the (x,z) plane and a quasi-stationary in the (x,y) plane were investigated. A better agreement concerning thermal kinetics was obtained with the quasi-stationary model, showing that conductive heat transfer in the y -direction is significant. In the transient model, the assumption of uniform energy distribution along the depth in the (x,z) model leads to a cylindrical weld profile different from the observed V-shaped weld but enable to reproduce the quenching effect near the root. Consequently, to overcome the limitations of both models, a 3D modelling using a volume z -dependent heat source would be required.

Concerning the metallurgical aspect, two sets of parameters deduced from dilatometric experiments in welding austenitizing conditions ($T_{\text{peak}} = 950^{\circ}\text{C}$ and $T_{\text{peak}} = 1200^{\circ}\text{C}$) were considered here. As a consequence, the theoretical and experimental hardness profiles were found in good agreement only in the region of HAZ close to these conditions. Therefore, to predict accurately the microstructure in the entire HAZ, precise dilatometric experiments established in different austenitizing conditions are required to take into account the grain growth effect.

Acknowledgments

The authors would like to express their gratitude to Michel Dumons and Jean Costa of the Université de Bretagne Sud for assisting with the development of the experimental part of this work. We are grateful to Rémi Bertet and Jean-Claude Parpillon of the Direction des Constructions Navales d'Indret (Nantes) where the welding experiments were carried out. We also thank Pierre Bocquet and Michel Gautier from the Centre de recherche des Matériaux du Creusot where the dilatometric experiments were performed. This work was partially supported by the Fonds Européen de Développement Régional (FEDER).

6. References

Andrews J.G., Atthey D.R., "Hydrodynamic limit to penetration of a material by a high-power beam", *J. Phys. D: Appl. Phys.*, vol. 9, 1976, p. 2181-2194.

- Arata Y., "Evaluation of beam characteristics by the ab test method", *Plasma, electron and laser beam technology*, Metals Park, Ohio/USA: American Society for Metals, 1986, p. 177-189.
- Carron D., Rogeon P. *et al.*, "Modelisation of metallurgical phase transformations in heat affected zone by using dilatometric experiments achieved in a EBW austenitizing conditions", *Mathematical modelling of weld phenomena 6* Eds H. Cerjak, H.K.D.H. Bhadeshia, Institute of materials, 2002, p. 391-409.
- Costantini M., *Simulation numérique du soudage par faisceau d'électrons. Contribution au développement d'un modèle prédictif de l'apport d'énergie*, Ph.D. dissertation, Univ. Paris 6, 1996.
- Dumord E., *Modélisation du soudage continu par faisceau de haute énergie : application au cas du soudage par laser Nd :YAG d'un acier X5 Cr.Ni 18-10*, Ph.D. dissertation, Univ. Bourgogne, 1996.
- Fabbro R., Chouf K., "Keyhole modeling during laser welding", *J. Appl. Phys.*, vol. 87, n°9, 2000, p. 4075-4083.
- Giedt W.H., Talerico L.N., "Prediction of Electron Beam depth of penetration", *Welding Research Supplement*, Dec, 1988, p. 299s-305s.
- Grignon C., Petitpas E., Pertinet R., Condoure J., « Modélisation thermométallurgique appliquée au soudage laser des aciers », *Int. J. Therm. Sci.*, vol. 40, 2001, p. 669-680.
- Jin Xiangzhong, Li Lijun, "An experimental study on the keyhole shapes in laser deep penetration welding", *Optics and Lasers in Engineering*, In press, 2003.
- Jüptner W., "Untersuchungen zum einbrandverhalten eines elektronenstrahls unter berücksichtigung der strahlgeometrie", *Genahmigte dissartation*, Univ. Hannover, 1975.
- Jüptner W., Franz Th., Sikau J., Sepold G., "Laser Interaction with Plasma during Material Processing", *Laser physics*, vol. 7, 1997, p. 202-207.
- Kaplan A., "A model of deep penetration laser welding based on calculation of the keyhole profile", *J. Phys. D: Appl. Phys.*, vol 27, 1994, p. 1805-1814.
- Ki H., Mohanty P.S., Mazumder J., "Modelling of high-density laser-material interaction using fast level set method", *J. Phys. D: Appl. Phys.*, vol 34, 2001, p. 364-372.
- Konkol P.J., Smith P.M., Willebrand C.F., Connor L.P., "Parameter study of Electron-Beam Welding", *Welding Journal*, Nov. 1971, p. 765-776.
- Kroos J., Gratzke U., Simon G., "Towards a self-consistent model of the keyhole in penetration laser beam welding", *J. Phys., D: Appl. Phys.*, vol. 26, 1993, p. 474-480.
- Leblond J.B., Devaux J., "A new kinetic model for anisothermal metallurgical transformations in steels including effect of austenite grain size", *Acta metall.*, vol.32, 1984, p. 137-146.
- Matsuhiro Y., Inaba Y., Ohji T. "Mathematical modelling of laser welding with a keyhole: modelling of laser welding (Part1)", *Welding International*, vol.8, n°4, 1994, p. 286-291.
- Matsunawa A., Semak V., "The simulation of front keyhole wall dynamics during laser welding", *J. Phys., D: Appl. Phys.*, vol. 30, 1997, p. 798-809.

- Miyazaki T., "Material removal produced by a high-power-density electron beam", *J. Appl. Phys.*, vol. 48, 1977, p. 3035-3041.
- Noller F., "The stationary shapes of vapor cavity and molten zone on EB-welding", 3rd *International Colloquium on welding and melting by electrons and laser beam, CISFFEL* Lyon, 1983, p. 89-97.
- Rabier S., Développement d'un modèle éléments finis pour la simulation d'écoulements à surface libre : application au soudage, Ph.D. dissertation, Univ. de Provence (Aix-Marseille I), 2003.
- Rogeon P., Couedel D. *et al.*, "Numerical simulation of electron beam welding of metals : Sensitivity study of a predictive model", *Mathematical Modelling of Weld Phenomena 5* Eds H. Cerjak, H.K.D.H. Badeshia - Institute of Materials, 1999, p. 913-943.
- Rosenthal D., "The theory of moving sources of heat and its application to metal treatments", *Trans. ASME*, vol. 48, Nov. 1946, p. 849-866.
- Semak V., Matsunawa A., "The role of recoil pressure in energy balance during laser materials processing", *J. Phys., D: Appl. Phys.*, vol. 30, 1997, p. 2541-2552.
- Semak V., Bragg W., Damkroger B., Kempka S., "Transient model for the keyhole during laser welding", *J. Phys., D: Appl. Phys.*, vol. 32, 1999, p. L61-L64.
- Solana P., Ocana J.L., "A mathematical model for penetration laser welding as a free-boundary problem", *J. Phys., D: Appl. Phys.*, vol. 30, 1997, p. 1300-1313.
- Van Schijndel A.W.M., "Modeling and solving building physics problems with FemLab", *Building and Environment*, vol. 38, 2003, p. 319-327.
- Wei P.S., Wu T.H., Chow Y.T., "Investigation of high-intensity beam characteristics on welding cavity shape and temperature distribution", *J. Heat Transfer*, vol. 112, 1990, p. 163-169.